Röttger J (1991) MST radar and incoherent scatter radar contributions to studying the middle atmosphere. *Journal of Geomagnetism and Geoelectricity* 43: 563–596.

Röttger J and Larsen MF (1990) UHF/VHF radar techniques for atmospheric research and wind profiler applications. In: Atlas D (ed.) *Radar in Meteorology*, pp. 253–281. Boston, MA: American Meteorological Society.

Woodman RF (1991) A general statistical instrument theory of atmospheric and ionospheric radars. *Journal of Geophysical Research* 96: 7911–7928.

Woodman RF and Guillen A (1974) Radar observations of winds and turbulence in the stratosphere and mesosphere. *Journal of the Atmospheric Sciences* 31: 493–505.

Precipitation Radar

S E Yuter, University of Washington, Seattle, WA, USA

Introduction

Precipitation radars are widely used to determine the location, size, and intensity of precipitating storms. Ground-based scanning precipitation radars are used in short-term weather and flood forecasting, and to estimate the distribution and amount of cumulative rainfall over a region. The weather services of many industrial countries have networks of operational radars that monitor precipitation near population centers. The output from these operational radar networks can be combined to provide a picture of the distribution of precipitation over synoptic-scale regions. Mobile precipitation radar on aircraft provides pilots with information to navigate safely around dangerous regions of hail and turbulence. Precipitation radars are also used to map the three-dimensional structure of storms. Spaceborne precipitation radar on low-orbit satellite maps the structure and distribution of precipitation around the globe over periods of months and years.

The British and Americans first developed weather radar during World War II. The precipitation radar transmits a pulse of electromagnetic energy via an antenna. When the transmitted energy encounters a reflector, such as a raindrop, part of the transmitted energy is scattered back toward the antenna, where it is received and amplified. The time delay between the original pulse transmission and the receipt of the backscattered energy is used to deduce the distance to the reflector. The relationship between the range-corrected, backscattered, returned power and the size and number of the reflecting targets is the physical foundation for interpreting precipitation radar data.

The frequency of electromagnetic waves f in Hz (s^{-1}) is defined as $f = c/\lambda$, where c is the speed of light and λ is the wavelength. Radar frequencies are divided into several bands, as shown in **Table 1**. The choice of frequency for precipitation radar is a tradeoff between the practical constraints of size, weight, cost, and the relation between the wavelength and the size of the target hydrometeors. Theoretical considerations favor the choice of the longer S-band and C-band wavelengths for many precipitation applications. However, use of these longer wavelengths is not always practical. The beam width for circular antennas is proportional to λ/d, where d is the antenna diameter. In comparison to shorter wavelengths, longer wavelengths necessitate a larger antenna to obtain a focused beam of the same angular beam width. Larger antennas are heavier, require more powerful motors to rotate them, and are more expensive than smaller antennas. Shorter X-, K_u-, and K_a-band wavelengths are often utilized in mobile precipitation radars deployed on spacecraft, aircraft, and ships where size and weight are more constrained as compared to stationary ground-based radars.

Table 1 Precipitation radar frequencies and wavelengths (adapted from Skolnik, 1990, and Rinehart, 1991)

Band designation	Nominal frequency (GHz)	Nominal wavelength (cm)	Applications
S	2–4	15–8	Surface-based radars
C	4–8	8–4	Mobile and surface-based radars
X	8–12	4–2.5	Mobile and surface-based radars
K_u	12–18	2.5–1.7	Mobile and spaceborne radars
K_a	27–40	1.1–0.75	Mobile and spaceborne radars

Precipitation Radar Components

The precipitation radar consists of a transmitter, receiver, transmit/receive switch, antenna, and display (**Figure 1**). In this simplified diagram, the processing of the electromagnetic signals into output suitable for display is included in the display block. A phase detector may be included to measure Doppler velocity. The radar transmitter contains a modulator that switches the transmitter on and off to form discrete pulses. The radar sends out a pulse and then switches to the receiver to listen. The range to the targets is obtained by comparing the time of pulse transmission to the time the backscattered pulse is received. In precipitation radars, the pulses are transmitted at a pulse repetition frequency (PRF) of $\sim$ 300–1300 Hz and each pulse is order 1 μs (10^{-6} s) in duration. The time between transmitted pulses limits the maximum range (r_{max}) the electromagnetic pulse can travel before the next pulse is transmitted (eqn [1])

$$r_{max} = \frac{c}{2PRF} \quad [1]$$

The receiver detects and amplifies the received signals and averages the characteristics of the returned pulses over defined time periods. Typical peak transmitted power for an operational precipitation radar is 10^5–10^6 W. Typical received power is 10^{-10} W. The transmit/receive switch protects the sensitive receiver from the powerful transmitter. Without the switch, the radar transmitter would burn out the receiver. In practice, the transmit/receive switch is not perfect and a small amount of transmitted energy leaks into the receiver.

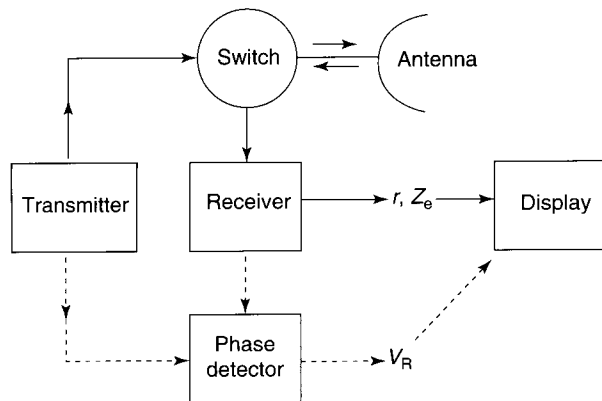Radar antennas focus transmitted energy and direct it along a narrow angular beam. For scanning radars, this direction is often described in terms of an elevation angle relative to the ground and an azimuth angle relative to north. Moving the antenna points the axis of the beam in different directions, and permits scanning of two- and three-dimensional regions of the atmosphere. The antenna shape determines the radar beam size and shape. The radar energy is maximum along the center of the beam and decreases outward with increasing angular width. The beam width is defined as the angular width where the power is exactly half the maximum power. Most precipitation radars utilize a circular parabolic antenna for both transmission and reception.

The main purpose of the display is to distinguish scatterers at different ranges. A basic scanning radar display will usually indicate the compass angle and range to the radar echo in polar coordinates. **Figure 2** shows the range-corrected received power as a function of range along a single pointing direction of the antenna. This example illustrates that not all the energy received at the radar is backscattered from meteorological targets. Transmitter leakage and ground clutter from nearby nonmeteorological targets such as trees and buildings are present at close ranges in the display. The signal from a point target such as a radio tower is present at 50 km range. The wider signal associated with meteorological echo is present in the range between 90 and 115 km.

The Radar Equation

The radar equation expresses the relationship between the transmitted power and backscattered received power from precipitation targets in terms of the radar's hardware characteristics and the distance between the transmitter and the target. In this section, the radar equation and radar reflectivity will be derived by first making some simplifying assumptions and then gradually refining the terms to more accurately represent the electromagnetic theory underpinning precipitation radars.

Isolated Scatterers

The amount of power incident (P_i) at an isotropic target of cross-sectional area A_t at range r_1 from an isotropic transmitter is given by eqn [2], in which P_t is the transmitted power (**Figure 3A**).

$$P_i = \frac{P_t A_t}{4\pi r_1^2} \quad [2]$$

Transmitted power and received power are commonly expressed in units of watts or dBm. The latter represents the ratio of power (P) in watts relative to 1 milliwatt ($10 \log_{10} [P/10^{-3}\,\text{W}]$). In a typical

Figure 1 Simplified hardware block diagram of a precipitation radar. The non-Doppler portion of the system yields the range r and equivalent reflectivity factor (Z_e) of the target. Dashed lines connect parts of the system included in a Doppler radar that additionally measures the radial velocity of the target (V_r). (Adapted from Houze, 1993.)
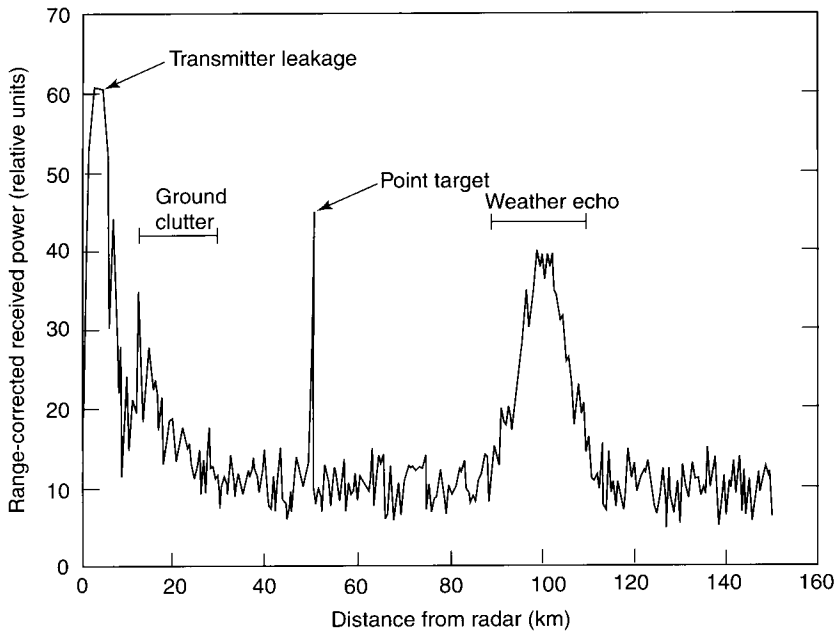
Figure 2 Two-dimensional radar display of range-corrected received power as a function of range showing signal from transmitter leakage, ground clutter, point target, and weather echo. See text for further details. (Adapted from Rinehart, 1991.)

operational precipitation radar, the minimum detectable signal is ~ -100 dBm and the peak transmitted power is ~ 90 dBm.

Assuming the target does not absorb any power and radiates the energy it receives isotropically, the power received at range r_2 from the target by a receiver of effective cross-sectional area A_e (**Figure 3A**) is given by eqn [3].

$$P_r = \frac{P_t A_t}{4\pi r_1^2} \left(\frac{A_e}{4\pi r_2^2}\right) \qquad [3]$$

When the transmitted energy is focused with an antenna, the ratio of the power per unit area along the axis of the focused beam to the power per unit area of an isotropic transmitter is a measure of antenna gain (G). For a circular, parabolic antenna typically used on precipitation radars, the antenna gain can be approximated in general as a function of the horizontal (θ_H) and vertical (θ_V) beam widths in radians, or for the receiving antenna as a function of the radar wavelength and A_e, as shown by the relationship [4].

$$G \approx \frac{\pi^2}{\theta_H \theta_V} \approx \frac{4\pi A_e}{\lambda^2} \qquad [4]$$

The antenna gain is usually of large magnitude and is often expressed in decibel units, $10 \log_{10} G$. For example, the antenna gain specification is 45 dB for the US National Weather Service WSR-88D operational radars, which means the antenna focuses energy about 30 000 times better than an isotropic transmitter. The use of a directional antenna for transmission leads to modification of the term representing trans-

mitted power in eqn [3] from P_t to $G_t P_t$, where G_t is the gain of the transmitting antenna. Usually precipitation radars utilize a single directional antenna for both transmitting and receiving which permits the simplifications of $r_1 = r_2 = r$ and $G_t = G$ in eqn [3].

Real-world scatterers are usually not isotropic, and the size of the backscattered cross-section area A_t is usually not equal to the physical size of the scatterer. The amount of scattered energy is dependent not only on the radar wavelength and incident power at the range of the target, but also on the target characteristics of size, shape, composition, three-dimensional angle between the target and transmitter, and target velocity. The backscattering cross-section (σ) is defined as the apparent area that, if scattered isotropically, would return to the receiver an amount of power equal to the power actually received. **Table 2** shows values for σ for diverse types of single scatterers.

Making substitutions for P_t, A_e, and A_t into eqn [3] yields eqn [5], which gives the power received by a precipitation radar with a directional antenna from a single target of backscattering cross-section σ at range r (**Figure 3B**).

$$P_r = \frac{P_t G^2 \lambda^2 \sigma}{(4\pi)^3 r^4} \qquad [5]$$

Distributed Scatterers

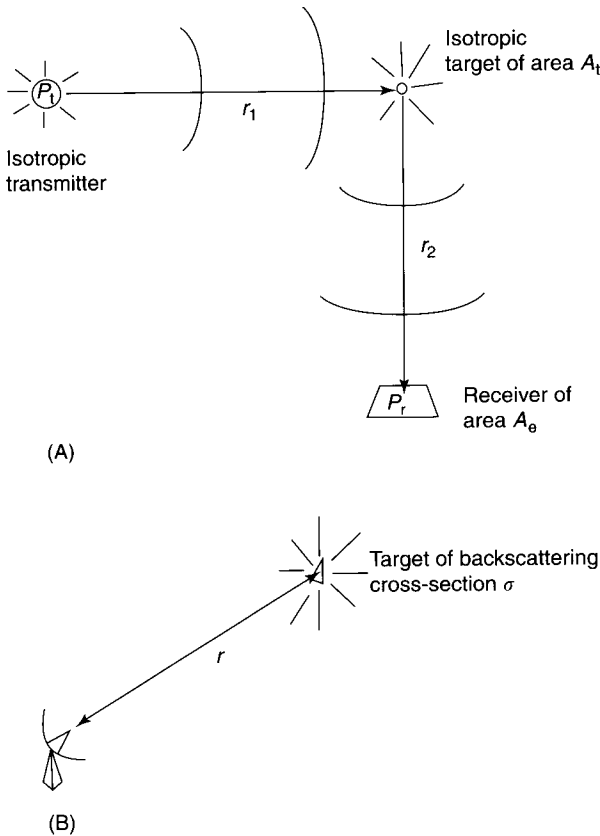Precipitation particles such as raindrops, snowflakes, hail, and graupel act as distributed scatterers in the

(A)

(B)

Figure 3 (A) Schematic of energy from an isotropic transmitter (P_t) traveling distance r_1 to an isotropic target of area A_t. The energy received at the target (P_r) is then isotropically radiated by the target and travels distance r_2 to a receiver of area A_e. (B) In precipitation radars, an antenna is used to focus the energy into a particular direction. The received energy is scattered by the target at range r. The backscattered portion of the energy corresponding to cross-section σ is received by the antenna.

volume of atmosphere illuminated by the precipitation radar. The resolution volume (V_{res}) illuminated by a transmitted pulse along the beam is approximated by a cylinder defined by the beam widths and pulse length of the radar hardware and the range to the volume, expressed as eqn [6].

$$V_{res} \approx \pi \left(r\frac{\theta_H}{2} \right) \left(r\frac{\theta_V}{2} \right) \frac{c\tau}{2} \qquad [6]$$

Table 2 Backscattering cross-sections at $\lambda = 10\,cm$ (adapted from Doviak and Zrnic, 1993)

Object	$\sigma\ (m^2)$
C-54 aircraft	10 to 1000
Human	0.14 to 1.05
Weather balloon, seagull	10^{-2}
Small birds	10^{-3}
Bee, dragonfly	3×10^{-6} to 10^{-7}
Water sphere ($D = 2\,mm$)	1.8×10^{-10}
Free electron	8×10^{-30}

Here τ is the pulse length in seconds. Antenna beam widths are assumed to be small, such that the small angle approximation $\theta \approx \sin\ \theta$ is valid. The resolution volume is defined as the incremental volume along the beam from which scattered energy is received simultaneously at the radar. The one-half pulse length factor (i.e., $\tau/2$) comes in since the backscattered energy from the front edge of the pulse at time $t_0 + \tau/2$ and range $r_0 + c\tau/2$ arrives back at the radar at the same instant as backscattered energy from the trailing edge of the pulse at time $t_0 + \tau$ and range r_0 (**Figure 4**). To account for the actual distribution of power within a beam generated by a circular parabolic antenna, a correction factor of $1/(2\ \ln 2)$ is applied to eqn [6] yielding eqn [7].

$$V_{res} = \frac{\pi r^2 \theta_H \theta_V c\tau}{16\ \ln 2} \qquad [7]$$

For operational precipitation radars, typical beam widths of 1–2° and pulse lengths of 0.5–1 μs result in resolution volumes of order 10^7–$10^8\,m^3$ at 60 km range.

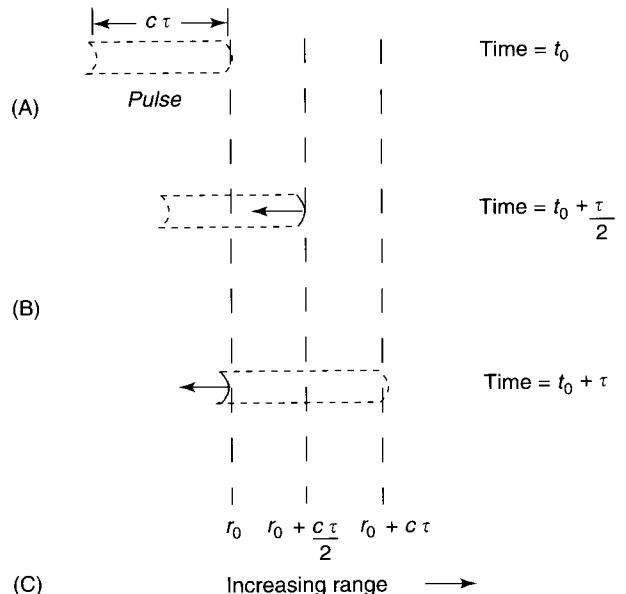The backscattered signal from a volume of randomly distributed scatterers is the sum of the signals

(A)

(B)

(C)

Figure 4 (A) The front edge of radar pulse of length $c\tau$ moving left to right reaches range r_0 at time $= t_0$. (B) At time $= t_0 + \tau/2$, the front edge of the pulse reaches range $r_0 + c\tau/2$. Backscattered energy from range $r_0 + c\tau/2$ moves to the left. (C) At time $t_0 + \tau$, the front edge of the radar pulse is at $r_0 + c\tau$. The backscattered energy from the front edge of the pulse which was at $r_0 + c\tau/2$ at time $t_0 + \tau/2$ is now at r_0 and arrives back at the radar simultaneously with the backscattered energy from the back edge of the pulse at r_0 at time $t_0 + \tau$.

scattered by each of the targets $\sum_{i=0}^{n} \sigma_i$. The summation of the backscattered cross-sections from precipitation scatterers in a unit volume is called the reflectivity and is defined as $\sum_{vol} \sigma_i$. As individual particles move with respect to one another within the resolution volume, the phase of the individual backscattered signal changes between pulses, and the summation of the signals varies slightly from pulse to pulse. The received power is usually averaged over 50 or more consecutive pulses to yield an estimate that is independent of the fluctuations. The final form of the radar equation implemented in the signal processors of precipitation radars combines eqns [5] and [7] and substitutes the radar reflectivity in the resolution volume, $V_{res} \sum_{vol} \sigma_i$, for σ. The radar processor calculates the averaged received power from the set of scatterers within the resolution volume at a particular range. Eqn [8] is a general form of the radar equation valid for scatterers of all sizes.

$$\bar{P}_r = \frac{P_t G^2 \lambda^2 \theta_H \theta_V c\tau}{1024(\ln 2)\pi^2 r^2} \sum_{vol} \sigma_i \qquad [8]$$

The 'gate spacing' parameter of the radar processor controls the number and spacing of individual reflectivity estimates along the radar beam. It can be set to a value that combines the signal from several consecutive resolution volumes to increase the effective volume over which the averaged returned power is computed (eqn [8]). In many radars, the pulse length τ, PRF, gate spacing, and the number of gates sampled (i.e., maximum range) are variables that can be modified by the radar operator. In scanning radars, the radar operator also specifies the set of elevation angles and range of azimuth angles to be illuminated by the antenna. The specification of the variable radar parameters is called the 'radar scan strategy'.

The spatial scale of the resolution volume is important in interpreting radar data, since electromagnetic sensors cannot distinguish the spatial distribution of scatterers within a volume. **Figure 5** shows six unit resolution volumes containing different spatial orientations of nine scatterers of the same material, shape, and size. Since radar reflectivity (eqn [12]) is only a function of the size and number of the scatterers per unit volume, the radar reflectivity values for all six volumes are equal. By convention, it is assumed that the beam is filled with uniformly distributed scatterers (**Figure 5A**). An important component of the radar design process is the balancing of the spatial scale of the features of interest and the physical characteristics of the sensor that determine the scale of the resolution volumes.
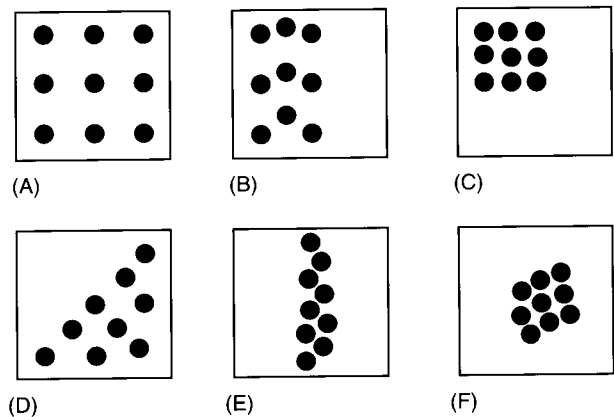

Figure 5 Set of six unit resolution volumes with the same radar reflectivity. All volumes contain the same number of identical targets. The spatial distribution of targets within a resolution volume is unknown and is usually assumed to be uniform.

Association of Radar Signal to Precipitation Characteristics

Radar Reflectivity of a Volume of Precipitation

To be of value in precipitation studies, the average returned power measured by the radar must be related to the physical characteristics of the precipitation particles within the resolution volume. The backscattering cross-section of a single water drop (σ_d) increases monotonically when the diameter D is less than $\sim \lambda/16$ according to [9], in which $|K|^2$ is the complex index of refraction

$$\sigma_d = \frac{\pi^5}{\lambda^4} |K|^2 D^6 \qquad [9]$$

Eqn [9] is referred to as the Rayleigh approximation of the backscattering cross-section. When the diameter of the drop, D, is greater than $\lambda/16$, Mie or optical scattering occurs. In contrast to Rayleigh scattering, under conditions of Mie scattering, the backscattered returned power fluctuates as the size of the scatterer increases (**Figure 6**).

For precipitation applications, it is preferable to use longer wavelengths to encompass as large a range of raindrop diameters as possible within the scattering regime where the Rayleigh approximation is valid. By definition, raindrops have diameters > 0.2 mm. Most rainfall in mid-latitudes consists of raindrops < 5 mm in diameter. Drops as large as 7 mm in diameter have been observed but are rare since large drops are unstable and tend to break up into smaller drops. The maximum raindrop diameter for which the Rayleigh approximation is valid is 6.25 mm for 10 cm wavelength and 3.13 mm for 5 cm wavelength, respectively.

Replacing σ_i with σ_d in eqn [8] yields the radar equation for spherical drops under conditions when
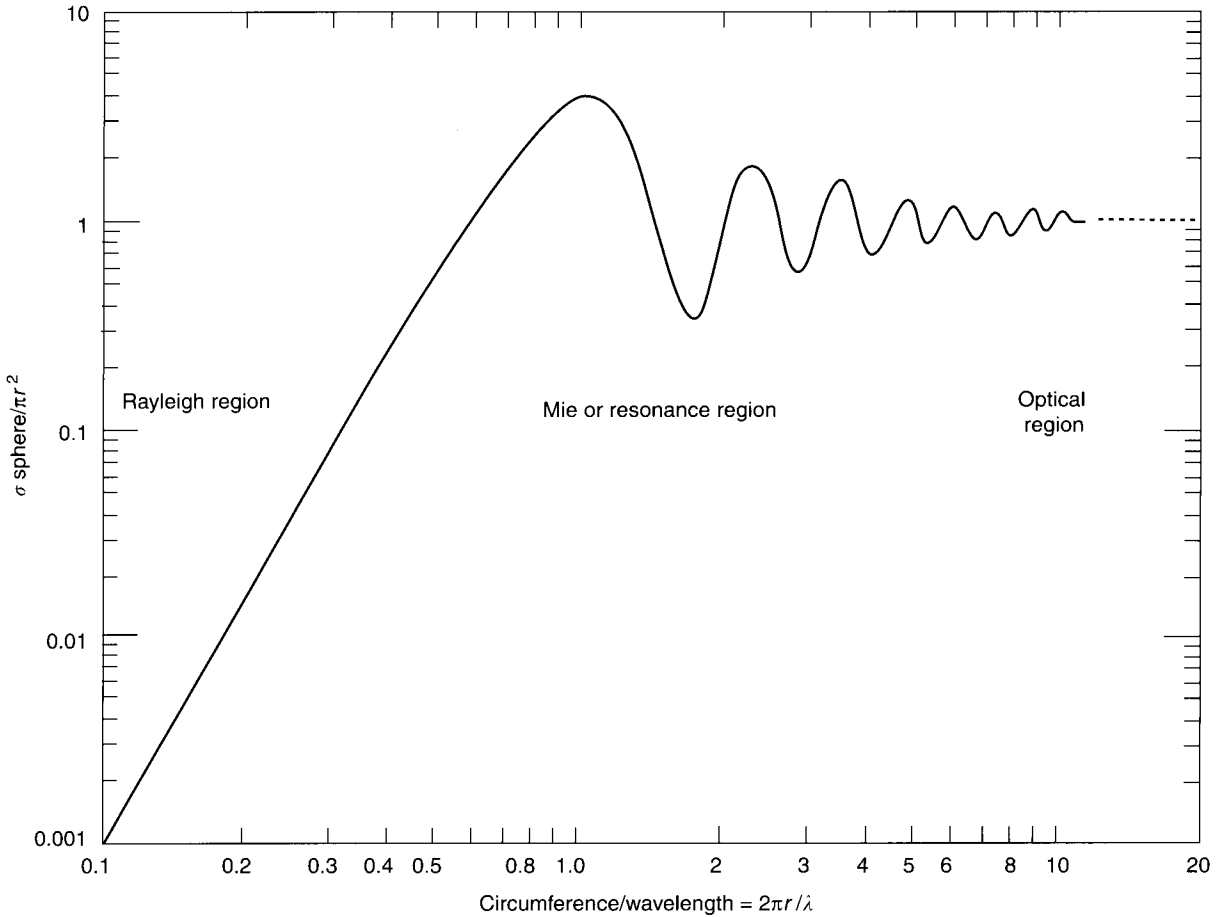
Figure 6 Normalized backscattering cross-section area of a perfectly conducting sphere as a function of circumference divided by radar wavelength λ. Since water drops are not perfectly conducting, the transition from Rayleigh to Mie scattering for the radar reflectivity of spherical water drops occurs at $2\pi r/\lambda \sim 0.2$. (From Skolnik, 1990.)

the Rayleigh approximation is valid (eqn [10]).

$$\bar{P}_r = \frac{P_t G^2 \lambda^2 \theta_H \theta_V c\tau}{512(2 \ln 2)\pi^2 r^2} \sum_{vol} \frac{\pi^5 |K|^2 D_i^6}{\lambda^4} \qquad [10]$$

Eqn [10] can be rearranged, as in [11], to group the numerical constants and parameters of the radar hardware together to form the 'radar constant' (C).

$$\bar{P}_r = \left(\frac{P_t G^2 \theta_H \theta_V c\tau\pi^3}{1024 \ln 2\lambda^2}\right) \frac{|K|^2}{r^2} \sum_{vol} D_i^6$$

$$= C\frac{|K|^2}{r^2} \sum_{vol} D_i^6 \qquad [11]$$

The radar reflectivity factor (Z) is defined by eqn [12].

$$Z = \sum_{vol} D_i^6 = \sum n_i D_i^6 = \int N(D)D^6 dD \qquad [12]$$

The discrete form of the definition in the middle is used in calculating Z from *in situ* measurements such as aircraft particle probes or disdrometers that resolve n_i, the number of drops per unit volume of atmosphere, in several discrete diameter intervals. In the continuous definition to the right, $N(D)$ is the number of particles per unit volume in the diameter range D to $D + dD$.

Rearranging eqn [11] yields the definition of Z in units of $mm^6 m^{-3}$ in terms of variables measured by the radar, and constants associated with the radar hardware and a particular gate spacing (eqn [13]).

$$Z = \frac{\bar{P}_r r^2}{C|K|^2} \qquad [13]$$

In evaluating eqn [13], a value is needed for $|K|^2$. Precipitation particles consist of water, ice, or a combination of the two. The complex index of refraction, $|K|^2$, is 0.93 for water and 0.197 for ice. Within a particular resolution volume of the radar, the individual meteorological scatterers contributing to Z

could be composed of water, ice, or melting ice. The scatterers could also include nonmeteorological targets such as insects, birds, and chaff (i.e., highly reflective man-made scatterers such as thin metal strips). There is no current method to be certain of the value of $|K|^2$. The convention is to assume that all the scatterers are composed of liquid water and to define the equivalent radar reflectivity factor Z_e according to [14].

$$Z_e = \frac{\bar{P}_r r^2}{C(0.93)} \qquad [14]$$

By this definition, a single spherical drop with a diameter of 1 mm within a 1 m^3 volume of air has $Z_e = 1$. Equivalent radar reflectivity factor is usually expressed in dBZ such that $dBZ_e = 10 \log_{10} (Z_e/1)$. It is common usage to refer to the display of dBZ_e values as 'radar reflectivity'. It is usually specified in context whether 'radar reflectivity' refers to dBZ or $mm^6 m^{-3}$ values. The difference between 30 dBZ and 20 dBZ is 10 dB, following the decibel convention. Typical ranges of radar reflectivity values in different types of precipitation are shown in Table 3.

The physical interpretation of radar reflectivity is more complicated in regions of echo containing mixed-phase particles than in regions containing exclusively snow or rain. Partially melted ice particles can have different electromagnetic properties compared to equivalent-sized particles of only ice or water. When snow melts within a narrow layer, a reflectivity maximum in the vertical associated with a concentration of partially melted particles can be discerned if the observing radar has sufficient spatial resolution and sensitivity.

Attenuation: Energy Losses along the Radar Beam

The path along the radar beam to the target resolution volume and back to the radar contains air molecules and possibly cloud and precipitation particles. These particles absorb and scatter the radar energy, reducing both the incident energy at the target and the backscattered energy arriving at the radar compared to what their values would be if the intervening medium were free space. The total power extracted from the wave is called attenuation, and is the sum of the power absorbed and the power scattered by the intervening particles. Attenuation is a function of radar wavelength, and the size, shape, and composition of the intervening particles. Attenuation accumulates as the wave moves from the radar to the target and back from the target to the radar. Following Beer's Law, the incremental reduction in received power with incremental distance ds caused by attenuation is given by eqn [15], in which $k_L(s)$ is the attenuation coefficient (in units of inverse length) over an incremental volume along a path centered at range s.

$$\frac{d\bar{P}_r}{ds} = -2k_L(s)\bar{P}_r \qquad [15]$$

Although $k_L(s)$ is called a coefficient, it is not a constant. Rather it represents the combined influences of attenuation by gases, cloud, and precipitation at a particular location described by range s. The factor 2 is needed since the radar energy travels the same path twice. The received power accounting for the attenuation is the integral solution of eqn [15] from ranges 0 to r. This can be expressed as [16], in which $\bar{P}_{ro}$ is the power that would have been received without attenuation.

$$\bar{P}_r = \bar{P}_{ro} \exp\left(-2 \int_0^r k_L(s)ds\right) \qquad [16]$$

Attenuation is often expressed as the ratio of the attenuated received power to the nonattenuated received power in units of dB km^{-1}. By utilizing the identity $\log_{10} X = 0.434(\ln X)$ and defining the specific attenuation as $k(s) = (10 \log_{10} e)k_L(s) = 4.34 k_L(s)$ in units of dB km^{-1}, eqn [16] becomes [17].

$$10 \log_{10} \frac{\bar{P}_r}{\bar{P}_{ro}} = 4.34 \left(-2 \int_0^r k_L(s)ds\right)$$
$$= -2 \int_0^r k(s)\, ds \qquad [17]$$

The specific attenuation can also be defined in terms of the drop size distribution, and the extinction cross-section, $\sigma_e(D)$, which represents the attenuation contributed by a particular particle size D, using the relationship [18], in which $N(D,r)dD$ is the number density of hydrometeors per particle size interval dD per unit volume within the incremental volume centered on range r.

$$k(r) = \int_0^\infty \sigma_e(D)N(D,r)\, dD \qquad [18]$$

Table 3 Typical values of observed radar reflectivity in various types of precipitation

Radar reflectivity (dBZ)	Associated precipitation types
−30 to 0	Marginally detectable precipitation
0 to 10	Drizzle, very light rain, light snow
10 to 30	Light to moderate rain and heavier snow
30 to 60	Moderate to heavy rain
40 to 55	Graupel
55 to 70	Hail
30 to 50	Melting snow particles

In practice, specific attenuation is often estimated as a function of the equivalent reflectivity without attenuation $Z_e(r)$. This can be represented by eqn [19], in which α and β are coefficients which are a function of the drop size distribution $N(D)$.

$$k(r) = \alpha Z_e(r)^\beta \qquad [19]$$

Eqn [16] and the definition for $k(s)$ can be incorporated into eqn [13] to yield eqn [20] for the radar reflectivity factor in situations where the attenuation is not negligible.

$$Z_e(r) = \frac{\bar{P_r} r^2}{C|K|^2} \exp\left(2 \int_0^r k_I(s)ds\right)$$

$$= \frac{\bar{P_r} r^2}{C|K|^2} \exp\left(\frac{2\alpha}{4.34} \int_0^r Z_e(s)^\beta \, ds\right) \qquad [20]$$

At radar wavelengths, attenuation by atmospheric gases is dominated by oxygen and water vapor absorption. Gaseous attenuation varies with the radar wavelength, path length, and depth of the troposphere penetrated by the radar beam. Two-way gaseous attenuation curves have been calculated using a standard atmosphere for a range of radar beam elevation angles and radar wavelengths. The overall effect of gaseous attenuation is small at S-band and C-band wavelengths, of order $0.01 \, \mathrm{dB \, km}^{-1}$ one way for a 10 cm wavelength radar, but increases as wavelength decreases. A correction for gaseous attenuation is usually made automatically in the radar's signal processor.

The attenuation caused by cloud droplets < 0.2 mm in diameter is dominated by absorption. For radar wavelengths ≥ 5 cm, attenuation by cloud particles is sufficiently minimal to be ignored. For X-band and K-band wavelengths, the one-way attenuation due to cloud droplets is of the order of $0.1 \, \mathrm{dB \, km}^{-1}$ per $\mathrm{g \, m}^{-3}$ liquid water content and is of sufficient magnitude to be of concern. However, unlike the situation with gaseous attenuation, there is no standard model for the distribution of cloud droplets as their distribution is discontinuous and chaotic. Because of the complexities in estimating the actual distribution of cloud particles along a particular radar beam, an automatic correction for attenuation by cloud particles is difficult to implement.

Attenuation in rainfall and snow is a function of the radar wavelength, temperature, particle type, and particle-size distribution. The attenuation in rain can be calculated as a function of reflectivity for specified drop size distributions, temperatures, and radar wavelengths as shown in **Figure 7** and **Table 4**. At reflectivities > 40 dBZ, which can occur within heavy rainfall, attenuation can become significant at C-band
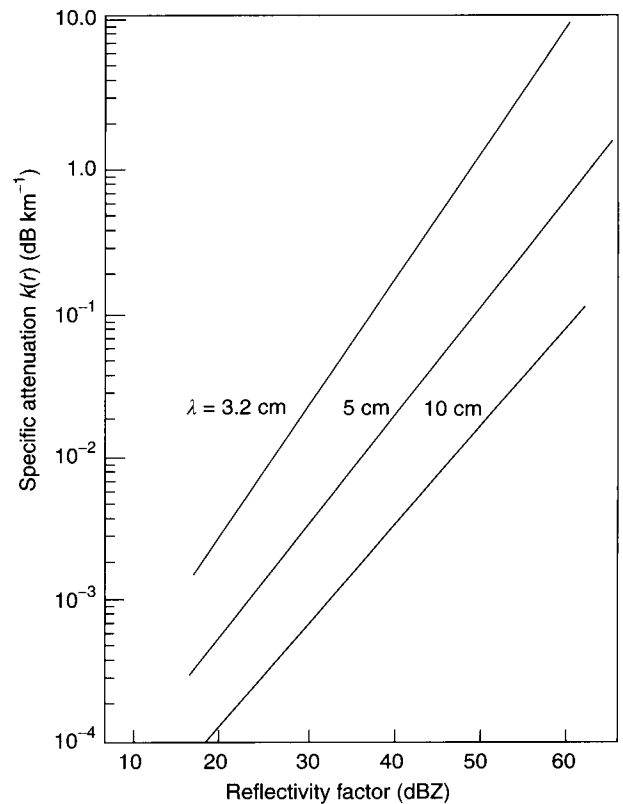

Figure 7 Specific attenuation versus radar reflectivity at $\lambda = 3.2$, 5, and 10 cm. Computations assume $T = 18°C$ and Laws and Parson drop size distribution. (Adapted from Doviak and Zrnic, 1993.)

and X-band. S-band energy can become significantly attenuated when passing through regions containing hail or exceptionally heavy rainfall ($Z > 55$ dBZ). **Figure 8** shows a comparison of X-band and S-band reflectivities obtained in a Florida squall line. While both radars are in reasonable agreement regarding the reflectivity pattern between the squall line and the radar, there is a significant difference in the reflectivity pattern behind the squall line. The attenuated X-band radar reflectivities indicate a much smaller area of precipitation and weaker intensities behind the squall line compared to the nonattenuated S-band data.

Attenuation in rain is usually difficult to correct automatically since the attenuation is a function of the

Table 4 Attenuation in rain for several wavelengths as a function of radar reflectivity (Z) at $T = 0°C$ (adapted from Battan, 1973)

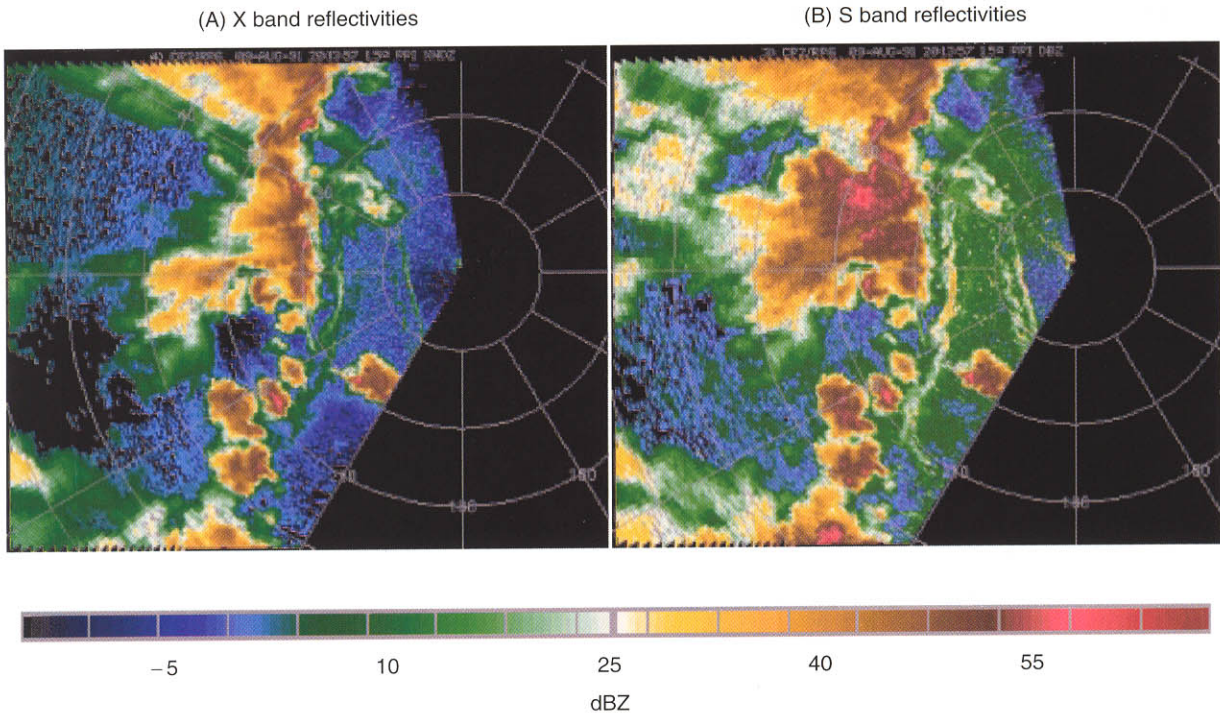| Radar wavelength (cm)	Specific attenuation in units of $dB \, km^{-1}$
2.0	$7.15 \times 10^{-4} \, Z^{0.725}$
3.21	$2.9 \times 10^{-4} \, Z^{0.72}$
5.5	$1.12 \times 10^{-4} \, Z^{0.62}$
10.0	$3.0 \times 10^{-5} \, Z^{0.62}$

Figure 8 Comparison of X- and S-band radar reflectivities in a 1.5° elevation angle scan obtained from the dual-frequency NCAR CP-2 radar on 9 August 1991 at 2013 UTC near Cape Canaveral, Florida. The strong reflectivities within the squall line to the west of the radar attenuate the X-band signal (A). The S-band reflectivity data (B) reveal a larger area of precipitation behind the squall line than does the X-band reflectivity data. Range rings are at 10 km intervals.

real rain field that is imperfectly measured because of attenuation. The rainfall attenuation correction is sensitive to the actual distribution of reflectivity and assumptions about the drop-size distributions along the radar beam. Under special circumstances, such as downward-pointing precipitation radars on aircraft and satellites, a reference reflectivity such as the reflectivity of the ocean surface can be used to estimate path-integrated attenuation. Surface reference and other methods to correct for attenuation at short wavelengths are a topic of active research. The reduction in reflectivity due to attenuation often has to be accounted for in the data interpretation.

Location of the Radar Beam in the Atmosphere

Standard Refraction

The classic formula for refraction is Snell's Law, which describes the bending of a light ray at the interface of two media. The ratio of the incident velocity of the wave (V_i) to the refracted velocity of the wave (V_r) is $V_i/V_r = \sin i / \sin r$, where i is the angle of incidence and r is the angle of refraction. In the Earth's atmosphere there is no interface, but the nonuniform vertical distribution of water vapor pressure and temperature refracts the radar beam, changing its direction of propagation compared to a radar beam in free space. The change in direction of the beam is defined in terms of the vertical gradient of the index of refraction dn/dh, where $n = c/v$, h is height, c is the speed of light, and v is the velocity of the wave in the medium. At precipitation radar frequencies for a standard atmosphere, $dn/dh \approx -4 \times 10^{-8}\,\mathrm{m^{-1}}$, sufficiently large to noticeably bend the radar beam downward compared to its free-space path. The negative value of dn/dh implies that v increases with increasing height.

If the index of refraction were constant with height or zero, the radar beam would curve upward with increasing range relative to the surface of the Earth because of the Earth's curvature. Precipitation radar data are usually interpreted in a ground-relative frame of reference. The following equation ([21]) for the height of the radar beam above the Earth's surface (h) takes into account both the refraction by a standard atmosphere and the curvature of the Earth.

$$h \cong h_0 - \frac{4}{3}R + \sqrt{r^2 + \left(\frac{4}{3}R\right)^2 + 2r\frac{4}{3}R \sin \varphi} \quad [21]$$

Here φ is the elevation angle of the radar beam, h_0 is the height of the radar antenna, r is the range from

the radar, and R is the radius of the Earth at the latitude of interest. **Figure 9** shows the radar beam paths for the set of elevation angles used by the US National Weather Service for scanning volumes of precipitation.

Nonstandard Refraction

The vertical distribution of water vapor pressure in the atmosphere is dependent on the vertical profiles of temperature and relative humidity. When moisture and/or temperature inversions are present, the vertical gradients of water vapor pressure, temperature, and the index of refraction differ from their standard atmosphere values and nonstandard refraction, also known as anomalous propagation, can occur. The most common type of nonstandard refraction is associated with a sharp vertical gradient in the index of refraction. In these circumstances the propagation path of the radar beam is bent downward more sharply than under standard atmosphere conditions. **Figure 10** shows the ray paths in arc distance coordinates, where a radar beam experiencing no refraction would be a straight line. The 0.4° elevation angle ray path traversing the inversion (solid line) is bent downward compared to a standard atmosphere ray path (dashed line). For very small elevation angles, nonstandard refraction can bend the ray path into the Earth's surface (**Figure 10**). Meteorological conditions associated with moisture and temperature inversions and hence nonstandard refraction include: nocturnal radiation cooling, advection of warm dry air over cooler bodies of water, and deposition of cool moist air at the surface by downdrafts in precipitating storms.

When the radar beam undergoes nonstandard refraction, the height of the radar resolution volume at a particular range is lower than it would be under conditions of standard refraction. A radar beam elevation angle that usually clears nearby mountain peaks may intersect them under conditions of nonstandard refraction. A radar echo at a mountain peak can be difficult to discern as a nonmeteorological echo associated with anomalous propagation, as it is common for orographic precipitation to form over mountain peaks. In the extreme case, when the ray path is pointed into the ground, a strong echo, associated with the large cross-section of the Earth's surface, appears on the radar display.

An example of anomalous propagation associated with a temperature inversion in the vicinity of Amarillo, Texas, is shown in **Figure 11A** within a 0.5° elevation scan. The majority of echo to the north and north west of the radar is nonmeteorological echo due to anomalous propagation. In regimes where real precipitation echoes usually have sufficient vertical extent to be illuminated by higher elevation angles in
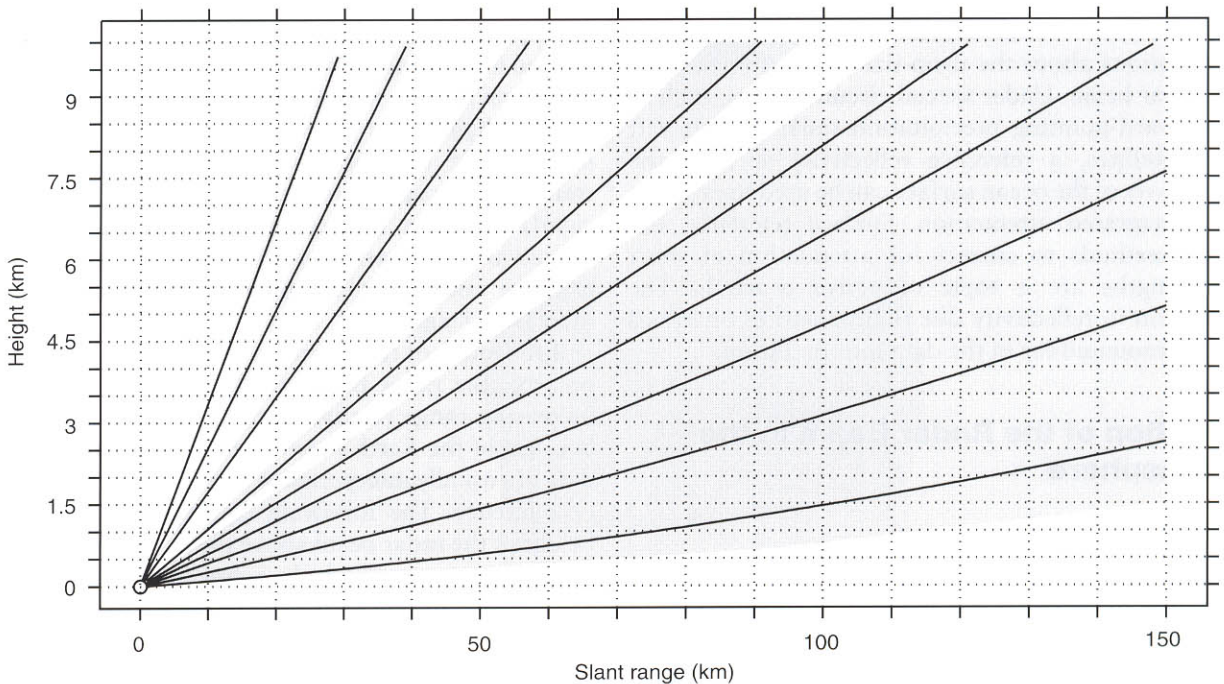
Figure 9 Radar beam center height (lines) and beam width (shaded) relative to the Earth's surface as a function of slant range for the US National Weather Service precipitation scan strategy (1° radar beam width and elevation angles: 0.5°, 1.45°, 2.4°, 3.35°, 4.3°, 6.0°, 9.9°, 14.6°, 19.5°). The radar location is indicated by the circle at 0 km height. Slant range refers to distance along the radar beam. Standard atmospheric refraction and the Earth's curvature have been taken into account to calculate the beam path following eqn [21].
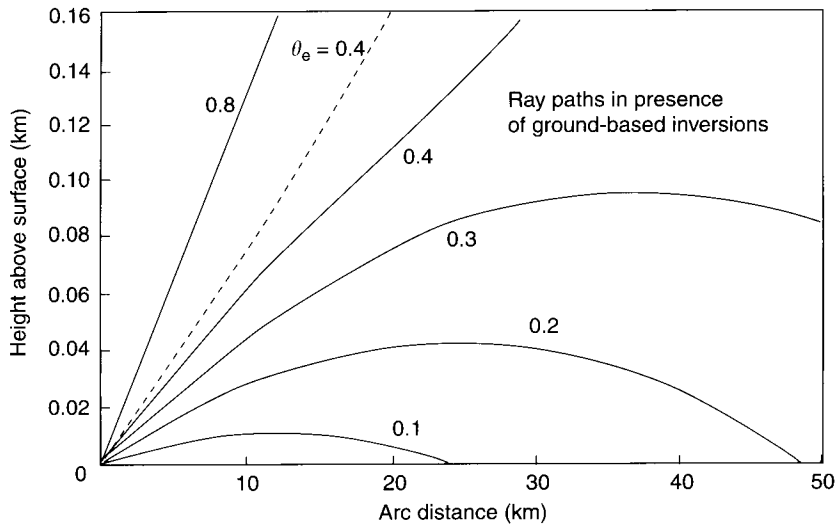
Figure 10 Ray paths (solid lines) in arc distance coordinates for radar beams of different elevation angles computed in an atmospheric model with a surface-based temperature inversion to 100-m altitude. The arc distance is the great circle distance along the surface of a sphere with a radius 4/3 times that of the Earth. The curvature of a sphere with a 4/3 Earth radius compensates for the standard refraction in the atmosphere such that in a height–arc distance coordinate system, a standard atmosphere ray path (i.e., no inversion) is nearly a straight line (dashed line). (From Doviak and Zrnic, 1993.)

the radar volume scan, a comparison between the lower and higher elevation angles can indicate a region of anomalous propagation. **Figure 11C** shows the elevation scan at 1.5° that contains a few isolated regions of precipitation to the northwest of the radar and a large region of precipitation between 60–240° azimuth. An algorithm that removes echo that does not have upward vertical continuity between consecutive elevation angles is applied in **Figures 11B,D** to the two elevation scans and removes most of the anomalous propagation. A characteristic of non-meteorological echo associated with anomalous propagation is that these echoes are relatively stationary compared to echoes associated with precipitating storms. A comparison of low elevation radar scans from several consecutive times can often reveal anomalous propagation. Automatic detection and removal of nonmeteorological echo associated with anomalous propagation is an area of ongoing research and includes methods involving polarization radar variables.

Polarization Variables Associated with Precipitation Estimation

Small raindrops, < 1 mm in diameter, are spherical. Larger raindrops are deformed by aerodynamics into horizontally oriented oblate spheroids. An oblate spheroid is the body of revolution formed when an ellipse with minor axis dimension (*a*) and major axis

dimension (*b*) is rotated about its minor axis. Raindrops usually fall with their maximum dimension oriented horizontally. This orientation may be temporarily disturbed by turbulence, drop collision, or aerodynamic instability. The ratio between the horizontal and vertical dimensions of larger drops results in different electromagnetic properties of the scattered energy when the incident energy is horizontally versus vertically polarized. A special type of precipitation radar, called a polarimetric radar, is designed to measure these properties by transmitting and receiving radiation in more than one orientation. Ongoing research has shown that polarization radar variables involving the differential amplitude and phase of the received power at orthogonal polarizations can be related to the physical characteristics of the precipitation. Of these variables, two commonly used in precipitation applications are differential reflectivity (Z_{DR}), related to the axis ratio of the precipitation particles, and specific differential propagation phase shift (K_{DP}), related to liquid water content.

Differential Reflectivity

To obtain radar reflectivity, energy is transmitted and received at the same polarization, usually horizontal. Differential reflectivity is the difference between the horizontally transmitted, horizontally received reflectivity factor (Z_{HH}) and the vertically transmitted, vertically received reflectivity factor (Z_{VV}). This is
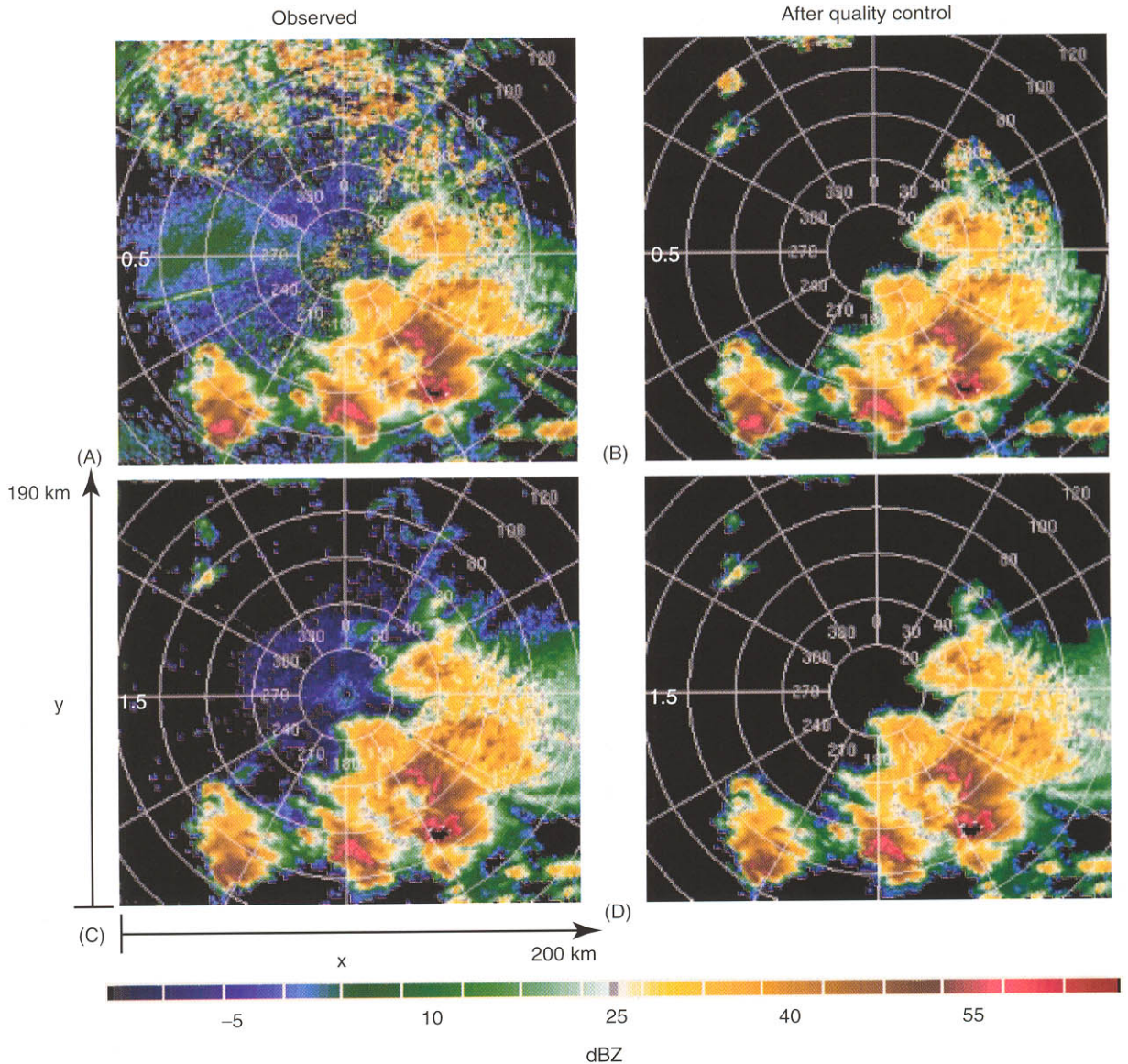
Observed

After quality control

Figure 11 Example of anomalous propagation in a volume scan from the US National Weather Service WSR-88D radar at Amarillo, Texas, on 25 May 1994 at 0029 UTC. The left column contains the observed data at 0.5° and 1.5° elevation angles and the right column shows the data after an automatic correction is applied to remove most of the anomalous propagation. The low level scan at 0.5° in (A) has a large area of nonmeteorological echo to the north and north west associated with anomalous propagation. See text for further details.

expressed in eqn [22].

$$ZDR = 10 \log_{10} \frac{Z_{HH}}{Z_{VV}} \qquad [22]$$

Differential reflectivity is a measure of the reflectivity-weighted mean axis ratio (a/b) of precipitation particles in a resolution volume. As raindrops increase in volume, D increases, the shape of the drop becomes more oblate, the axis ratio decreases, and the associated Z_{DR} value increases. For spherical raindrops or spherical ice particles, the axis ratio $a/b = 1$ and $Z_{DR} \sim 0$. The exact functional relationship between drop size and axis ratio in natural rain is a topic of active research. Of particular importance to precipitation studies is the capacity of Z_{DR} obtained at nearly horizontal elevation angles to distinguish among regions containing rain, hail, and graupel, and the layer of melting snow particles above the rain layer. **Table 5** presents typical Z_{DR} values associated with several basic precipitation types. Z_{DR} is also a function of the dielectric constant and hence composition of the particle. For a given axis ratio, the Z_{DR} value of a raindrop will be larger than for an ice particle. Graupel and hail particles are usually axially symmetric with an associated Z_{DR} value near zero. Negative values of

Table 5 Typical ranges of observed differential reflectivity values in several types of precipitation (adapted from Doviak and Zrnic, 1993; Straka et al., 2000)

Differential reflectivity (dB)	Associated precipitation types
− 0.5 to 0.5	Marginally detectable precipitation
− 0.5 to 0.5	Drizzle, very light rain, light snow
>1	Moderate rain and heavier snow
0.5 to 4	Moderate to heavy rain
− 2 to 0.5	Hail and graupel
0.5 to 4	Melting snow particles

Z_{DR} have been reported for regions containing hail and graupel, but the detailed physics underlying these measurements is not well understood. Melting snow appears to the radar as large particles with the dielectric properties of water. These particles often have very large axis ratios and large Z_{DR} values.

Differential reflectivity is independent of the absolute radar calibration since it is the difference between Z_{HH} and Z_{VV}, but it is sensitive to relative calibration. In practice, Z_{HH} and Z_{VV} are often measured by parallel hardware with different calibration constants, necessitating two calibration measurements. When viewed vertically, raindrops of all sizes appear circular and have an associated Z_{DR} value equal to zero. A Z_{DR} bias, accounting for the relative difference in calibration between the H and V polarizations can be estimated by pointing the radar beam directly upward in rain.

Differential Phase Variables

As an electromagnetic wave traverses a precipitation-filled volume, incident energy is scattered back toward the radar and forward along the beam. The forward scattered (propagated) component of the wave becomes shifted compared to the free-space component of the wave transmitted from the radar. Within horizontally oblate raindrops, the propagating horizontally polarized wave undergoes a larger phase shift per unit length and travels more slowly than the vertically polarized wave. After passing through a volume filled with horizontally oblate raindrops, the horizontally polarized wave will have a larger propagation phase shift than the vertically polarized wave (**Figure 12**). The one-way differential propagation phase (ϕ_{DP}) is defined in eqn [23] as the difference between the propagation phase shift of the horizontally transmitted, horizontally received energy (ϕ_{HH}), and the propagation phase of the vertically transmitted, vertically received energy (ϕ_{VV}).

$$\phi_{DP} = \phi_{HH} - \phi_{VV} \qquad [23]$$

As the radar wave traverses a region of precipitation filled with oblate drops, ϕ_{DP} accumulates with in-creasing range. To remove range effects, ϕ_{DP} is differentiated with respect to r to yield specific differential propagation phase (K_{DP}) in units of $\deg \text{km}^{-1}$ (eqn [24]).

$$K_{DP} = \frac{d\phi_{DP}}{dr} \qquad [24]$$

Often measurements of ϕ_{DP} are noisy and K_{DP} is integrated over several kilometers to obtain a usable signal.

K_{DP} values can be related to the liquid content and axis ratio of the drop by eqn [25], in which D_m is the maximum drop size, a/b is the axis ratio, and C_j is an empirically determined constant which is 0.5987 for $\lambda = 3.21$ cm and 0.05717 for $\lambda = 10.71$ cm.

$$K_{DP} = \lambda \int_0^{D_m} D^3 C_j (1 - a/b) N(D) \, dD \qquad [25]$$

The inverse proportionality of the constant C_j to wavelength outweighs the λ term in eqn [25] such that for a given liquid water content, K_{DP} increases with decreasing radar wavelength within the precipitation radar frequency band. K_{DP} is not affected by attenuation since it is based on the measurement of the phase shift of the wave rather than the amplitude of the returned power. This basis on phase shift allows a K_{DP} signal to be obtained when the radar beam is partially blocked, such as in mountainous terrain. Applications of K_{DP} include distinguishing the rain portion of rain/hail mixtures and estimating the liquid water content of oblate raindrops. A disadvantage of K_{DP} is its insensitivity to precipitation composed of small spherical raindrops, where $D < 1$ mm and $a/b = 1$, associated with low liquid water contents and low rain rates. **Table 6** presents typical S-band K_{DP} values of several basic precipitation types.

Precipitation Characterization and Estimation from Radar Data

Small-Scale Storm Structure

The two- and three-dimensional spatial and temporal patterns of radar-observed variables contain valuable information about storm structure and evolution that is used in many types of precipitation forecasting and research applications. In regions of vigorous upward motion, precipitation particles increase their mass primarily by accretion of smaller ice and water particles. These precipitation particles fall out as localized heavy showers, typically a few 100 m to 5 km in horizontal dimension, and appear on radar as localized vertically oriented regions of enhanced reflectivity called cells (**Figure 13A**). In mature and
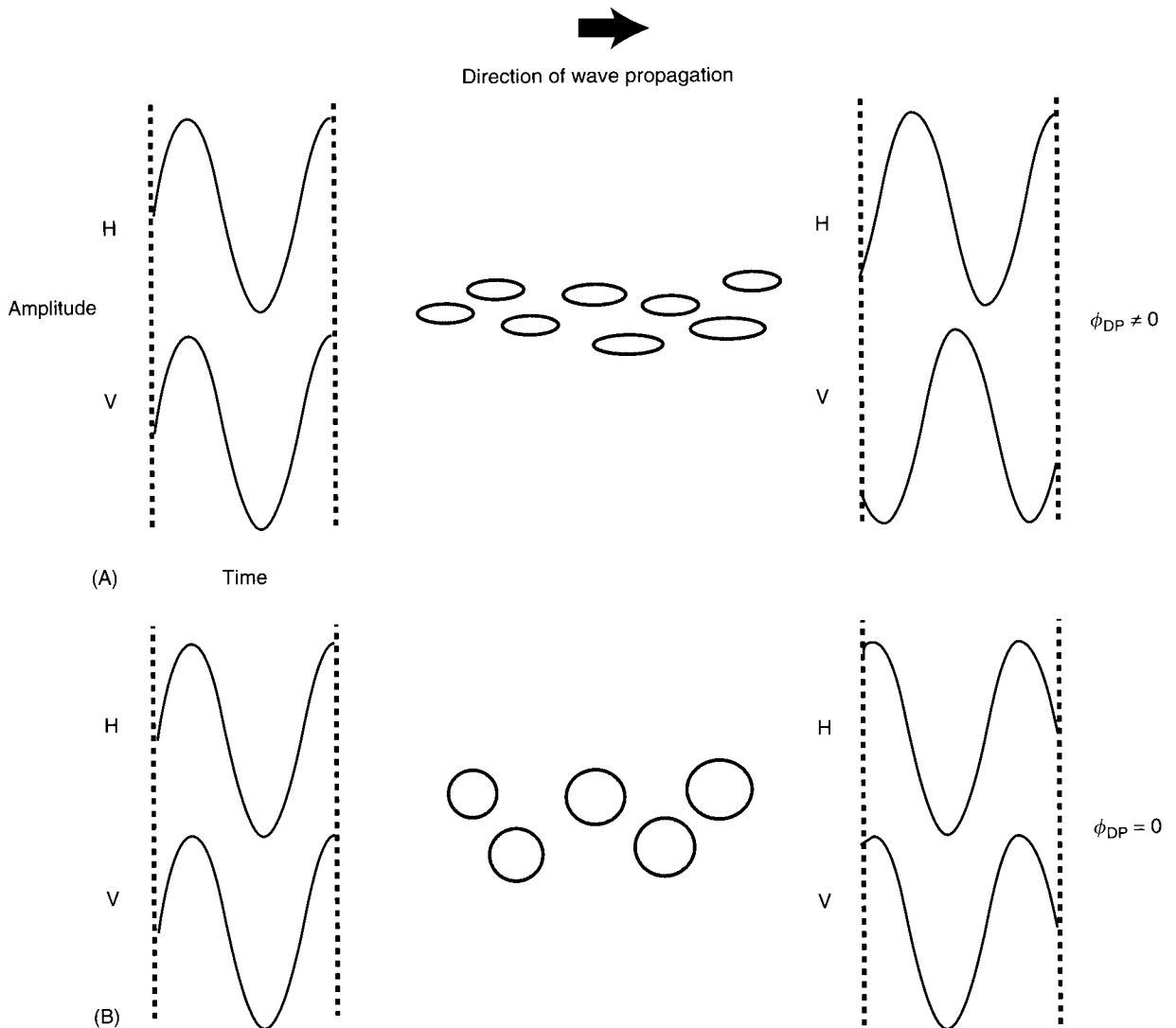
Direction of wave propagation

Figure 12 Sketch of the propagation phase shift of horizontally and vertically polarized electromagnetic waves passing through a precipitation-filled volume. For simplicity, the horizontally (H) and vertically (V) polarized waves are assumed to be in phase prior to entering the volume. (A) When the waves encounter horizontally oblate raindrops, the phase of the horizontally polarized wave is shifted more than the vertically polarized wave. (B) When the waves encounter spherical particles such as small raindrops or hail, the horizontally polarized wave and vertically polarized wave are shifted the same amount and $\phi_{DP} = 0$.

decaying convection, vertical motions are weaker, and precipitation particles may grow by vapor deposition. The associated radar echo has weak horizontal gradients of reflectivity and may exhibit a horizontal layer of enhanced reflectivities called the radar 'bright band' associated with a layer of melting particles (Figure 13B).

Figure 14 shows high spatial resolution X-band radar reflectivity data obtained by an aircraft radar over the tropical Pacific Ocean. The vertically oriented reflectivity maximum is tilted by a sloping updraft within the cell. A faint radar bright band is discernible to the right of the cell where ice particles generated in the cell are falling in an environment of weak vertical

velocity and melting in a thin layer. Detection of the bright band by radar is a function of both the physical properties of the melting layer and the sensitivity and spatial resolution of the radar. In radars with coarser spatial resolution, a weak bright band, as shown in Figure 14, would not be detectable.

Rainfall Mapping with Precipitation Radar: Role of the Raindrop Size Distribution

As described in the sections above, measured precipitation radar variables can be related to several parameters of the raindrop size distribution $N(D)$. The raindrop size distribution is generally accepted to be a truncated exponential function of the form [26],

Table 6 Typical ranges of observed S-band K_{DP} values in several precipitation types (adapted from Doviak and Zrnic, 1993; Straka et al., 2000; Bringi and Chandrasekar, 2001)

K_{DP} (deg km^{-1})	Precipitation types
− 0.5 to 0.5	Marginally detectable precipitation
− 0.5 to 0.5	Drizzle, very light rain, snow
− 0.5 to 1	Moderate rain
0.5 to 5	Moderate to heavy rain
− 0.5 to 1	Hail
− 0.5 to 1	Melting snow particles

in which D is the diameter of a spherical drop with volume equal to that of the actual raindrop, μ has a value between –3 and 8, D_o is the median volume diameter of the distribution, and N_o is a function of D_o, μ, and the total drop concentration.

$$N(D) = N_o D^{\mu} \exp\left(-3.67 D/D_o\right) \quad [26]$$

Drop size distributions and drop shapes have been measured and modeled. These studies have yielded a range of values for and a range of relationships among N_o, D_o, μ, and the drop axis ratio as a function of D. These uncertainties translate into uncertainties in relations among parameters of $N(D)$.

Moments of the drop size distribution (DSD) can be related to one another by an equation of the form $y = \alpha x^{\beta}$, where x and y are different moments of the

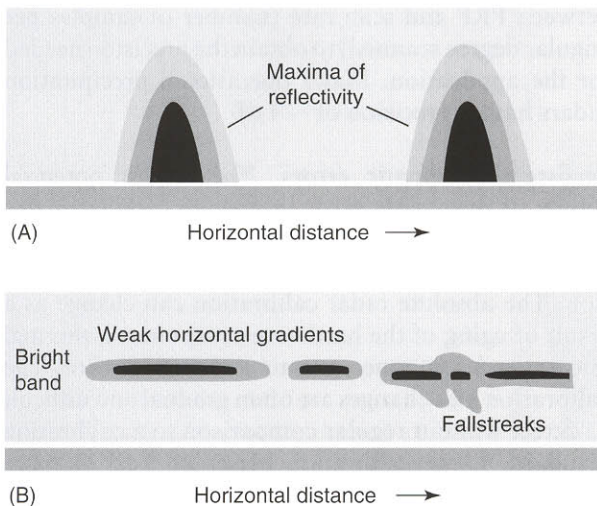(A)   Horizontal distance ⟶

(B)   Horizontal distance ⟶

Figure 13 Schematics of radar echo for vigorous convective and mature and decaying convection. (A) Vertical cross-section of vertically oriented reflectivity maxima associated with vigorous convection. (B) Vertical cross-section of layered reflectivity structure associated with mature and decaying convection. Fallstreak particle trajectories and reflectivity signatures tend to curve in vertical cross-section as a result of the combination of horizontal wind and particle descent. Darker shading indicates progressively higher radar reflectivity value. (From Houze, 1997, with permission of the American Meteorological Society.)

DSD, and α and β are real-valued coefficients. **Table 7** lists several moments of the DSD. The most commonly applied association between moments of the DSD is the Z–R relation, which translates the variability of the DSD as measured by the radar in terms of Z in mm^6 m^{-3}, into variability in terms of the desired quantity R in mm h^{-1}. The Z–R relation is traditionally expressed in the form $Z = aR^b$, although Z is the independent variable. **Figure 15** shows a plot of four commonly used Z–R mappings based on different empirical data sets, methodologies, and assumptions regarding the coefficients in eqn [26]. The Z-conditional relative uncertainty in rain rate varies from $\sim$ 10–50% as a function of Z for the four Z–R relationships in **Figure 15**. These Z-conditional uncertainties represent a combination of several error sources and differences in precipitation among regions. Z–R methods usually truncate input Z at $\sim$ 55 dBZ to mitigate large errors in estimated rain rate associated with hail.

Alternate methods to map rainfall using S-band and C-band radar data utilize measurements of Z_{DR} and K_{DP} in addition to, or in place of, Z. K_{DP} is related to the fourth moment of the DSD and can be used to estimate R using a power law of the form $y = \alpha x^{\beta}$. Other methods employ several simultaneously measured parameters of the DSD to constrain the coefficients in eqn [26]. The derived DSD is used in turn to estimate the desired parameter R. Several assumptions, with attendant uncertainties, are needed to make the associations among the polarimetric radar-measured bulk properties and the functional form of the DSD. Use of either Z_{DR} or K_{DP} to constrain the DSD coefficients requires assumptions about the drop axis ratio as a function of D. Neither Z_{DR} nor K_{DP} is sensitive to the small spherical drops within the DSD, so the distribution of the smaller drops must be assumed as a function of the derived distribution of the larger oblate drops. Additional assumptions regarding the variability of the coefficients in the DSD, particularly μ, are often utilized.

Practical Issues Contributing to Rain Map Uncertainty

The quantitative estimation of errors associated with rain mapping from radar data is severely hampered by the lack of an independent, precise, and accurate value with which to compare, and by rapidly changing conditions within precipitating storms that make it difficult to repeat a measurement under the same conditions. The discussion of uncertainty in rain mapping below is in terms of independent sources of random and systematic error (**Table 8**) for Z–R relations. Error sources for polarimetric methods are similar with a few exceptions. Z_{DR} and K_{DP}
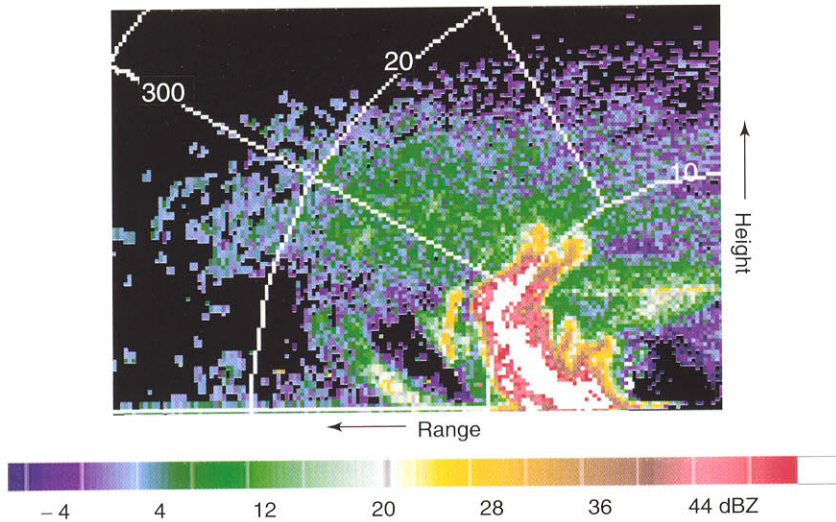
Figure 14 X-band radar cross-section through a vigorous convective cell in the tropical western Pacific warm pool obtained by NOAA WP-3D aircraft on 15 December 1992 at 2046 UTC. Range rings are at 10 km intervals and the radar gate spacing is 75 m. A faint radar bright band is indicated to the right of the convective cell. Reflectivities behind the cell (to the left) are attenuated.

measurements are not biased by the presence of hail. K_{DP} is not influenced by attenuation. Both Z_{DR} and K_{DP} are sensitive to mild nonstandard refraction such that the height of the radar beam is lower in the atmosphere compared to its height in a standard atmosphere. Methods using polarimetric variables can detect when the nonstandard refraction is sufficiently strong such that the radar beam intersects the ground.

Random errors The relative movement of individual scatterers within the resolution volume produces fluctuations in $\bar{P}_r$. Additionally, noise is associated with the receiver hardware. Individual samples of P_r containing these noise sources must be averaged to determine $\bar{P}_r$ within an acceptable uncertainty. The

degree of independence between consecutive samples is a function of the radar's wavelength, PRF, resolution volume size, and the spread of velocities within the resolution volume. For typical precipitation radars, consecutive samples are usually not independent. At higher PRFs, more samples are needed to yield an equivalent number of independent samples compared to a lower PRF. These constraints lead to compromises between PRF and scan rate (number of samples per angular degree scanned) to obtain the precision needed for the application. Many operational precipitation radars have a precision of ~ 1 dB.

Persistent systematic errors The largest potential source of systematic error in precipitation estimates derived from radar reflectivity is often calibration. Most precipitation radars are calibrated at installation. The absolute radar calibration can change as a result of aging of the hardware components, thermal effects, and component repair and replacement. The calibration bias changes are often gradual and difficult to detect without regular comparison to a calibration standard. Large calibration biases of 5 dB or more ($>100\%$ error in rain rate) are common in some operational radar networks. Careful calibration with a standard noise source can yield accuracies to within ~ 2 dB ($\sim 40\%$ error in rain rate). Calibration bias can also be estimated by comparing radar reflectivity data to suitable sample sizes of independent measurements such as: spatially scaled and temporally averaged point measurements of rainfall, reflectivity from a well-calibrated radar for matching volumes of atmosphere, or polarization measurements such as

Table 7 Moments of the drop size distribution related to rainfall estimation

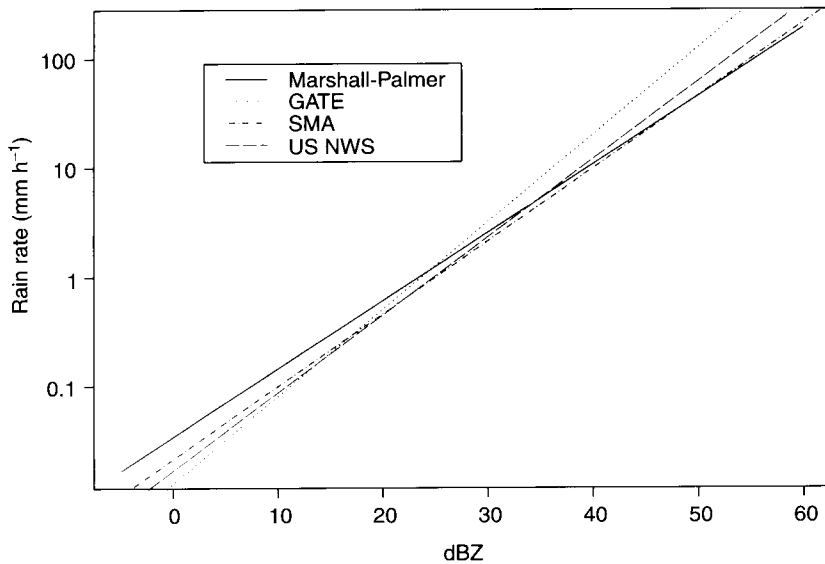| Measured or estimated property	Functional form in terms of N(D)
Total drop concentration (m^{-3})	$N_t = \int_0^\infty N(D)\, dD$
Radar reflectivity factor ($mm^6\, m^{-3}$)	$Z = \int_0^\infty N(D) D^6\, dD$
Liquid water content ($mm^3\, m^{-3}$)	$W = \frac{\pi}{6} \int_0^\infty N(D) D^3\, dD$
Rainfall rate ($mm\, h^{-1}$)	$R = \frac{3.6\pi}{6000}$ $\times \int_0^\infty N(D) D^3 V(D, T, P)\, dD$ in which $V(D, T, P)$ is the particle fall speed, which is a function of the diameter of the particles, air temperature, and pressure.

Figure 15 Plot of reflectivity versus rain rate for several Z–R relations: Marshall–Palmer ($Z = 220R^{1.6}$), GATE ($Z = 230R^{1.25}$), Swiss Meteorological Agency default (SMA, $Z = 315R^{1.5}$), and the US National Weather Service default (USNWS, $Z = 300R^{1.4}$).

K_{DP}, that are independent of the power calibration of the radar.

Another source of systematic error is associated with the changes in the DSD between the lowest available radar measurement and the ground. These variations are dependent on precipitation structure and typically vary in magnitude from 0 to ~ 3 dB km^{-1}. The magnitude of these errors increases with range when the variation with height is nonzero, since the height of the radar beam above the ground increases with increasing range (i.e., **Figure 9**). This type of error can be corrected using suitable vertical profiles of reflectivity or rain rate associated with the precipitation and storm type at each pixel. Errors associated with changes in DSD with height can be either positive or negative. Drier air at low levels may evaporate precipitation up to 100% and light rain falling through low stratus or fog may be enhanced up to 25%.

Ground clutter and shielding interfere with radar-derived rainfall mapping since a reliable estimate of returned power from meteorological targets is not available for the affected regions. Once identified, data corresponding to resolution volumes containing ground clutter from hills, buildings, towers, and trees close to the radar are usually set to 'missing' or 'not available'. Nearby mountains can block the radar beam, completely shielding the regions behind them. For radars sited in mountainous regions, a substantial portion of the potential 360° radar coverage area may be shielded. In instances where the beam is only partially blocked, a phase measurement such as K_{DP} may be used to estimate rain rate contingent on the limitations of that variable.

Systematic errors associated with intermittent conditions The existence and magnitude of some types of systematic error are a function of whether specific intermittent conditions are present. If these conditions are recognized, the bias in rain rate associated with them can be corrected. The identification within a radar scan of such intermittent conditions is an active area of research. Severe anomalous propagation can be identified and mild anomalous propagation can be corrected if atmospheric soundings are available. The high bias in rain rate associated with mistaking the reflectivity of hail for that of rain can be corrected if the hail is identified by use of a Z_{DR} or K_{DP} measurement.

If reflectivities within the melting layer are used as input to a Z–R relation for rain, the rain rates will be overestimated. The electromagnetic properties of melting particles increase the reflectivity signal by several dB compared to the reflectivity of the equivalent completely melted particles. These errors can be large, even when only a portion of the radar beam intersects the melting layer.

Other intermittent conditions associated with systematic errors are harder to identify, such as non-meteorological echo from migrating birds. Uncertainties in rainfall mapping are also associated with downdrafts and updrafts since the relations between moments of the DSD, such as a Z–R relation, are usually derived for still air conditions. In the presence of strong downdrafts, the fall speed of raindrops is increased relative to a stationary horizontal surface. For a given instantaneous reflectivity, apparent rain rate over a finite interval of time is increased from its still air value. The opposite is true for updrafts. At low levels, regions of high reflectivity are almost always

Table 8 Factors contributing to uncertainties in rainfall mapping from precipitation radar data. The magnitude of the effects is for operational scanning radars with typical resolution volumes of 1 km^3. The trend in uncertainty with increasing range is defined in terms of the same meteorological or nonmeteorological circumstance being present at closer versus farther ranges from the radar (adapted with permission of the American Meteorological Society from Austin, 1987)

Type of error	Factor	Nature of effect and situations where it is significant	Trend of uncertainty with increasing range from radar
Noise	Precision of measured $\bar{P}_r$	Varies with PRF and scan rate; typically ~ 1 dB	Not a function of range
Persistent bias	Calibration of $\bar{P}_r$	Typically ~ 2 dB for calibrated radars; depends on priorities and resources	Not a function of range
Persistent bias	Changes in DSD between lowest radar measurement and the surface	Varies between 0 and 3 dB km^{-1} depending on vertical structure of precipitation	Generally increases with height difference between lowest radar beam and the ground; increases with range
Persistent bias	Ground clutter and beam blockage	Varies with radar site and its relation to regional geography	Shielded area increases with increasing range
Intermittent bias	Signal enhancement by melting particles	Partially melted particles have Z values 1–5 dB larger than completely melted particles	Effect limited to ranges where radar beam intersects melting layer
Intermittent bias	Anomalous propagation	Associated with temperature and moisture inversions. Changes beam height in relation to its standard atmosphere value. In extreme, beam intersects ground yielding high Z value	Magnitude increases with smaller beam elevation angles, increasing range, and increasing strength of inversion
Intermittent bias	Nonmeteorological echo such as sea clutter, birds, and insects	Increases Z above its meteorological value. In extreme, indicates presence of heavy rain when there is none present	Generally decreases with range, as beam is located higher from near surface sources
Intermittent bias	Presence of hail	Increases measured Z to value 4–10 dB higher than that of associated rainfall	Decreases once resolution volume becomes larger than pocket of hail
Intermittent bias	Strong downdrafts	Increase R for same Z. Equivalent to reducing Z by 3–5 dB	Decreases once resolution volume becomes larger than downdraft
Intermittent bias	Attenuation	Reduces measured Z from its actual value. Increases with decreasing wavelength. Varies with distribution of precipitation along radar beam	Accumulates with range
Intermittent bias	Z-conditional variations in the DSD	Often difficult to isolate from other systematic errors. Uncertainty equivalent to variations in $Z \leq 2.5$ dB	Decreases with increasing size of resolution volume

associated with downdrafts. Since radar data used for estimating rainfall is usually obtained at low levels, downdrafts prevail over updrafts as a source of systematic error in rainfall estimation.

Two types of attenuation can impact radar-rainfall mapping: attenuation of the radar signal by hydrometeors in the atmosphere as described above, and attenuation caused by wetting of the radome covering the radar's antenna. The latter type includes both a power loss and a phase shift. The variability of the water film on the radome makes wet radome attenuation difficult to correct.

Other potential sources of uncertainty Uncertainty in rain mapping associated with beam filling is not related to a systematic error in measured reflectivity. Rather it is a result of the breakdown of the uniformly filled beam assumption used to interpret electromagnetic sensor data. For example, when an isolated 1 km^3 raining cell is contained within an otherwise empty 8 km^3 resolution volume, the measured reflectivity for the entire resolution volume will be much smaller than the reflectivity within the isolated raining cell. When the resolution volume is not uniformly filled (i.e., rain is not homogeneous in the volume), an uncertainty arises when computing the average rain rate from the average reflectivity. The reason is that while $y = \alpha x^\beta$, $\bar{y} \neq \alpha \bar{x}^\beta$ for $\beta \neq 1$, as is usually the case for Z–R relations. This type of uncertainty is of concern when computing R from Z for volumes that

are larger than the scale of the rainfall variability and when comparing different moments of the DSD obtained at different spatial resolutions, for example, ground-based radar and satellite passive microwave measurements, or radar and rain gauge data.

Evaluation of Radar-Derived Rain Maps

Independent evaluation of radar-derived rain maps using surface *in situ* measurements such as rain gauges and disdrometers have several sources of uncertainty. Sample volume sizes observed by precipitation radar are often $\sim 10^7$–10^9 times as large as those observed by a rain gauge or disdrometer. The combination of the scale variance of radar-measured variables and the use of measurements obtained at different scales yields large uncertainties. Variation of DSD with height contributes additional systematic error in direct comparisons between radar data above the surface and surface instrumentation. An assumption is usually made relating the nearly instantaneous radar measurement aloft to a time interval of the surface measurements below. Even when the rain gauge and radar are well sited and calibrated, discrepancies in rainfall estimates are often large. Gauge-to-radar discrepancies can increase with increasing small-scale variance of rainfall, e.g., isolated showers compared to widespread precipitation. A multiyear comparison of daily rain gauge versus radar-derived rain rates in Switzerland yielded an average error of $\sim 100\%$ (equivalent to $\sim 4.5\,\mathrm{dBZ}$) for areas of $1\,\mathrm{km}^2$. Error magnitude, in terms of standard deviation, is inversely proportional to the square root of the number of independent samples. Shortening the time interval for comparison between radar and rain gauge from 1 day to $1\,\mathrm{h}$ increases uncertainty in the surface point measurements by approximately a factor of 5 (i.e., $1/\sqrt{1/24}$). Alternatively, use of 30 day rainfall totals instead of daily totals from a single gauge or use of daily totals from 30 radar-gauge pairs decreases uncertainty by a factor of ~ 5 (i.e., $1/\sqrt{30}$).

To be useful in evaluation of radar-derived quantitative precipitation estimates, the systematic and random errors in the independent estimate need to be smaller than the systematic and random errors in the radar-derived estimate. Suitably large, averaged data sets of surface rain gauge and disdrometer measurements have been successfully used to evaluate corrections for large sources of error in radar-rainfall mapping such as calibration offsets, the variation of DSD with height, and the presence of nonrain hydrometeors such as hail and the melting layer. However, smaller magnitude uncertainties, such as the real-time Z-conditional variation of DSD, are difficult to isolate and quantify using rain gauge and disdrometer networks since very extensive networks are required.

See also

Radar: Cloud Radar; Doppler Radar; Incoherent Scatter Radar; MST and ST Radars and Wind Profilers; Meteor Radar; Synthetic Aperture Radar (Land Surface Applications).

Further Reading

Atlas D (ed.) (1990) *Radar in Meteorology*. Boston: American Meteorological Society.

Battan LJ (1973) *Radar Observation of the Atmosphere*. Chicago: University of Chicago Press.

Bringi VN and Chandrasekar V (2001) *Polarimetric Doppler Weather Radar*. Cambridge: Cambridge University Press.

Doviak RJ and Zrnic DS (1993) *Doppler Radar and Weather Observations*. New York: Academic Press.

Houze RA (1993) *Cloud Dynamics*. New York: Academic Press.

Meneghini R and Kozu T (1990) *Spaceborne Weather Radar*. Norwood: Artech House.

Rinehart RE (1991) *Radar for Meteorologists*. Fargo: Ronald E. Rinehart.

Skolnik MI (ed.) (1990) *Radar Handbook*. New York: McGraw-Hill.

Synthetic Aperture Radar (Land Surface Applications)

R K Vincent, Bowling Green State University, Bowling Green, OH, USA

Introduction

Synthetic aperture radar (SAR) images are produced by an active system that sends a microwave signal from a sensor platform to the ground and detects backscattered waves that the ground reflects directly back to a receiver on the same platform, which can be borne aloft by either airplanes or satellites. When the source and receiver are on the same platform, the radar is said to be monostatic. If the source and receiver are on different platforms, the radar is said to be bistatic. Commercial SAR systems are monostatic and always collect images to the side of the flight path of the sensor